Lawrence Berkeley National Laboratory

LBL Publications

Title

Towards bend-contour-free dislocation imaging via diffraction contrast STEM

Permalink

https://escholarship.org/uc/item/6tc7495t

Authors

Zhu, Yuanyuan

Ophus, Colin

Toloczko, Mychailo B

et al.

Publication Date

2018-10-01

DOI

10.1016/j.ultramic.2018.06.001

Supplemental Material

https://escholarship.org/uc/item/6tc7495t#supplemental

Peer reviewed

eScholarship.org Powered by the California Digital Library University of California

Towards bend-contour-free dislocation imaging via diffraction contrast STEM

Yuanyuan Zhu[a,*], Colin Ophus[b], Mychailo B. Toloczko[a], and Danny J. Edwards[a]

[a.] Energy and Environment Directorate, Nuclear Sciences Division, Pacific Northwest National Laboratory, Richland, WA 99352, USA
[b.] National Center for Electron Microscopy, Molecular Foundry, Lawrence Berkeley National Laboratory, Berkeley, California 94720, USA

Abstract

Dislocation imaging using transmission electron microscopy (TEM) has been an invaluable tool for characterizing crystallographic defects in metals. Recent advances in electron microscopy techniques have allowed for new dislocation imaging techniques to be devised. Compared to conventional TEM imaging, diffraction contrast imaging scanning transmission electron microscopy (DCI STEM) can provide better defect contrast with almost negligible bend contour artifacts, enabling more effective analysis of dislocation structures. Here we outline a simple procedure to help set up DCI STEM experiments, using a body-centered cubic HT-9 ferritic/martensitic alloy as an example. To study the behavior of dislocation imaging in STEM mode, we compared the imaging parameters in DCI STEM mode to corresponding conventional TEM images. We found that using a few milliradians of STEM convergence and collection semi-angles, $\boldsymbol{\alpha}$s and $\boldsymbol{\beta}$s, alleviates bend contours by averaging out the rocking-curve oscillation in reciprocal space. Practical guidelines regarding STEM parameters and specimen orientation and thickness are provided for DCI STEM dislocation imaging. Lastly, we show that coupling DCI STEM with spectrum images of Electron Energy Loss Spectroscopy and of Energy-dispersive X-ray Spectroscopy offers a comprehensive characterization of crystallographic defects and chemical information of complex microstructures.

Keywords: STEM, Dislocation image, Diffraction contrast, Reciprocity, Bend contour

1. Introduction

Ever since the first direct observation of dislocations in transmission electron microscopy (TEM) [1, 2], dislocation imaging has grown to be one of the most important characterization tools in the study of crystalline materials. The ability to directly image dislocations is critical to materials research, in particular metallurgy, given the direct relationship between dislocations and their effect on mechanical and physical properties. Dislocation evolution plays a critical role in thermomechanical processing of metallic materials, but dislocations also evolve due to other externally applied thermal and/or mechanical stresses or irradiation with energetic particles. In each case, it is important to understand how the material properties change due to the evolution of dislocations and their interaction with other microstructural features in the material.

For decades, dislocation analysis has been in the purview of conventional TEM (CTEM), supported by well-developed theories and simulations for understanding the contrast of dislocations in CTEM micrographs. However, with the recent advent of scanning transmission electron microscopes with more intense probes and faster, higher resolution detectors, there is

a renewed interest in using convergent-beam scanning transmission electron microscopy (STEM) to image dislocation structures [3, 4]. Development of STEM has already demonstrated advantages in many other characterization applications, including the determination of dislocation core structure [5], high-resolution mapping of lattice strain fields [6], and even in *in situ* environmental imaging [7]. Similarly, as early as the 1970s several groups reported on the promising potential of dislocation imaging using STEM as an alternative to CTEM [3, 8-12]. Among the advantages, the alleviation of bend contour contrast under certain STEM conditions greatly aids in the analysis of dislocations in dense fields of extended defects such as (sub-)grain boundaries or precipitates, especially ones that exhibit a strain field. Although previous studies have proven that, with proper parameters, DCI STEM satisfies the dynamical theory of diffraction contrast including the $\boldsymbol{g} \cdot \boldsymbol{b}$ criteria in CTEM [3, 8], it has not been clear how DCI STEM suppresses bend contours nor how different STEM parameters affect the contrast of dislocation images.

To answer these questions, we have investigated the image formation process in STEM mode for dislocation imaging and why bend contours can be alleviated in this imaging mode. In particular, DCI STEM imaging parameters such as convergence angle, camera length, objective aperture, and detector type, as well as the influence of the orientation and thickness of a body-centered cubic (BCC) ferritic alloy specimen, were systematically explored to evaluate their effects on image contrast and to provide practical guidelines for DCI STEM dislocation imaging. Finally, we propose a STEM-based comprehensive defect characterization approach.

2. Experimental procedures

2.1. Specimen preparation

TEM samples were prepared from an unirradiated BCC HT-9 ferritic alloy (composition and heat treatment are provided in Table 1) using an FEI Quanta 3D focused ion beam (FIB)/SEM. FIB lamellae (5 × 5 μm wide) were extracted using a 30 keV Ga beam for the initial thinning and lift-out, then welded to a gold-coated Cu half grid, and then thinned to approximately 200–300 nm using a 5 keV beam followed by a 2 keV step. Final thinning to ~100 nm or less was conducted using a flash electropolishing technique that effectively removes FIB-induced "black-spot" artifacts. The flash polishing is performed using a glass beaker with a cathode of stainless steel sheet that surrounds the walls of the beaker. An Au-coated grid with the TEM lamella is held by an Au-coated self-closing tweezer in an electrolyte in the beaker. The electrolyte, a solution of 5% perchloric acid in methanol, was cooled to 213 K. The flash polishing was conducted at 12 volts DC in 50 ms steps until the desired thickness was achieved in the thinnest region near the Pt cap. With optimized flash electropolishing recipe for HT-9 alloys, the final sample was largely free of black-spot damage and surface oxidation (Figure S1). A manuscript describing this flash electropolishing technique is in preparation.

Table 1. Composition and heat treatment of the HT-9 alloy for this study.

Heat Treatment	Composition (wt%)							
	Cr	C	Si	Mn	W	V	Mo	Ni
1038°C/5 min/air cool (AC) + 760°C/30 min/AC	11.9	0.2	0.23	0.5	0.5	0.34	1.02	0.58

2.2. Diffraction contrast imaging STEM

A simple way to begin the design of a DCI STEM experiment for a given sample is to convert the conventional unit of reciprocal vector, 1/Å, to milliradians (mrad). This conversion directly facilitates the determination of two key DCI STEM parameters: the probe convergence semi-angle and the collection semi-angle. Figure 1 illustrates the on-zone electron diffraction patterns used to plan the DCI STEM dislocation imaging performed in this work. First, based on the Laue equation, the angle between the direct beam and a diffracted beam is

$$\alpha = 2 \arcsin\left(\frac{\lambda g}{2}\right)$$

$$\alpha \approx \lambda g$$ [13]

where α is the divergence semi-angle in radians, λ is the electron beam wavelength in Å, and *g* is the reciprocal length of a given lattice spacing in 1/Å. To convert a reciprocal length *g* from 1/Å to mrad, one just needs to multiply it by a conversion ratio of approximately 1000λ. For example, for the primary energy of 200 kV used here, the conversion ratio *R* is a constant, ~25.1. Other conversion ratios for typical TEM primary energies are listed in Table S1 in the supplementary information.

Next, using the above 200 kV conversion ratio, the $1\mathbf{g}_{011}$ — the shortest spacing between the direct transmitted spot and the first-order diffraction spots of this BCC crystal — can be converted from 0.493 1/Å into 12.4 mrad (Figure 1b). To avoid interference effects caused by STEM disc overlapping, the upper limit of the STEM convergence semi-angle in this case needs to be <6.2 mrad. For most commercial microscopes, the STEM convergence angle can be readily tuned by selecting different second-condenser (C2) apertures. However, this provides a finite set of individual convergence angles without changing the excitation of the C2 and objective lenses. For the JEOL ARM200F microscope used in this work, only the smallest C2 aperture (physical diameter = 10 μm) meets the above requirement, providing a convergence semi-angle of 6.2 mrad. In the case of crystals with large lattice parameters on a low-index zone, if the built-in C2 aperture is not small enough to avoid disc overlap, one may consider switching to a lower primary energy or adjusting the C2 and objective lens currents to obtain the desired semi-convergence angle. Alternatively, the user can select a more distant **g** vector (e.g., the $1\mathbf{g}_{002}$ in Figure 1b) if it satisfies the imaging conditions. However, the latter is usually at the expense of a longer extinction distance (details will be discussed in Section 3.2).

Lastly, the range of STEM bright-field (BF) and annular dark-field (ADF) collection angles can be determined based on the radius of the direct disc and the values of high-order **g**-vectors in mrad, respectively. The criterion for the outer semi-angle of a BF detector is straightforward; ideally, the BF detector should capture only the transmitted beam; hence, it is preferred to be smaller than the radius of the direct disc, i.e., < 6.2 mrad in this case. The lower limit of the BF collection semi-angle will be discussed in Section 3.1. For the ADF collection range, to satisfy pure dark-field imaging and to maximize the collection of diffraction signals, it is ideal to exclude the direct disc while including the strong low-order diffraction discs. For example, in Figure 1b, to include the $1\mathbf{g}_{011}$ to $3\mathbf{g}_{011}$ discs in the collection range of the ADF detector, we chose the camera length (CL) that offers an inner semi-angle between 6.2 and 18.6 mrad, and an outer semi-angle ≥ 43.3 mrad; (note that the disc radius needs to be added to the $3\mathbf{g}_{011}$ vector to include the entire diffraction disc). From a practical standpoint, an on-zone STEM diffraction (Figure 1b) is recommended, and together with superimposed virtual BF and ADF detectors (can't be directly seen on a microscope's fluorescent screen), it can be used as a blueprint to construct DCI STEM imaging conditions.

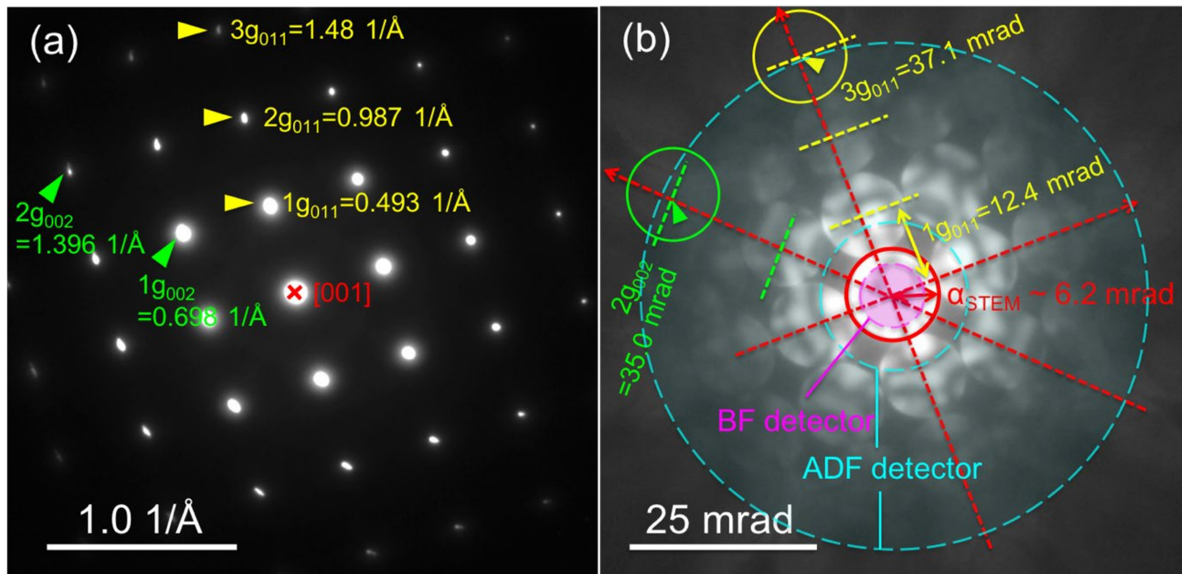

Figure 1. Planning DCI STEM experiment using electron diffraction. (a) The TEM selected area electron diffraction (SAED) pattern of the BCC HT-9 alloy along the <001> zone axis. (b) The STEM stationary diffraction under the same conditions with a convergence angle of 6.2 mrad (STEM disc radius). Based on the 1/Å-to-mrad conversion for the 200 kV primary energy used in this work (Table 1), the values of the reciprocal vectors for $\mathbf{g}_{001}$ and $\mathbf{g}_{002}$ are converted and marked in (b) in mrad for reference. Virtual BF and ADF detectors are superimposed on the STEM on-zone diffraction to aid the visualization of the signals collected for the formation of DCI STEM images.

2.3. Experimental setup

All CTEM and DCI STEM imaging experiments were conducted on a cold field-emission JEOL ARM200CF microscope operated at 200 kV, equipped with a hexapole type probe Cs-corrector (CESCOR, CEOS). The instrument is configured with a Gatan 965 Dual electron energy loss spectroscopy (EELS) system and a JEOL Centurio energy-dispersive x-ray spectroscopy (EDS) detector. DCI STEM dislocation images were acquired in a systematic row diffraction condition with the foil tilted away from [001] zone axis to approximately 1$\mathbf{g}_{011}$ on Bragg with a small positive $\mathbf{s}_\mathbf{g}$ [3] (noted as $\mathbf{s}_{1\mathbf{g}} > 1$ in Figures), with a 10 µm diameter C2 aperture corresponding to a 6.2 mrad convergence semi-angle, were used throughout the work unless stated otherwise. To facilitate direct comparison, a magnification of ×250,000 balancing between the size of field of view and probe scanning stability, a dwell time of 16 µs and 2048 pixel × 2048 pixel image size were used for all DCI STEM images. The collection semi-angles tested for the DCI STEM imaging are listed in Table 2, and the best CL and corresponding collection ranges for the ferritic alloy imaged in this work are marked by asterisks. Objective apertures of 5.5 mrad and 15.6 mrad were also applied to some DCI STEM-ADF imaging. Stationary STEM diffraction patterns were obtained by parking the STEM probe at the center of the field of view. Note that the stationary STEM diffraction patterns, although sample a much smaller volume than that of SAED in CTEM, they reflect the local foil thickness as well as the local diffraction conditions at the parked position of the STEM probe. The STEM scanning direction were adjusted in DigiScan to align STEM images with the corresponding CTEM images of the same field view to aid in direct comparison. For CTEM dislocation imaging, it was carried out in a similar systematic row diffraction condition to the DCI STEM in BF imaging mode, and the standard weak-beam dark-field (WBDF) mode with an objective

aperture radius of 5.5 mrad. A selective area diffraction aperture of 600 nm was employed during electron diffraction after the aperture was aligned to the center of the CTEM images. All the images shown in this paper are raw data with no post-acquisition smoothing or filtering.

STEM-based zero-loss EELS spectrum imaging was conducted using a convergence angle of 27.4 mrad, a CL of 1.5 cm for the Gatan imaging filter (GIF) camera, a GIF aperture of 5 mm, and energy dispersion of 0.25 eV/channel. EELS thickness maps were generated by a Log-ratio (absolute) routine [14] carried out in Gatan DigitalMicrograph software (GMS 3.0) using an effective atomic number of 26 for the iron-based specimen. For STEM-based EDS, a silicon drift detector with a detection area of 100 mm allowing a large solid angle (~0.98 sr) was used to acquire the X-ray signals. STEM-EDS spectrum images were recorded and processed using the dedicated EDS software Pathfinder (ThermoFisher Scientific).

Table 2. Camera length and corresponding STEM-BF and -ADF collection ranges for the ARM200CF microscope operated at 200 kV. Asterisks mark the best CL and corresponding collection ranges for the ferritic alloy imaged in this work.

Camera Length (cm)	BF collection outer semi-angle (mrad)		ADF collection semi-angles (mrad)
	No aperture	1 mm aperture	
12	30	3.8	45–180
20	18	2.3	27–110
***40**	*9	1.1	*14–55
80	4.5	0.8	6.8–28
120	3	0.6	4.5–18
150	2.4	0.3	3.6–15

3. Results and discussion

3.1. How DCI STEM imaging mode suppresses bend contours

During the early development of STEM imaging in 1960s, the principle of reciprocity was often invoked to interpret the image contrast [15, 16]. As schematically illustrated in the ray diagram in Figure 2a, reversing the electron beam propagation in BF-TEM mode (in blue) provides an immediate appreciation that the BF-STEM mode (in orange) could be equivalent to CTEM if the TEM incidence semi-angle (i.e., any initial divergence of the incident beam) is close to the STEM collection semi-angle ($\boldsymbol{\alpha}_T \approx \boldsymbol{\beta}_S$) and the TEM collection semi-angle is similar to the STEM convergence semi-angle, $\boldsymbol{\beta}_T \approx \boldsymbol{\alpha}_S$. In practice, a much larger STEM collection angle $\boldsymbol{\beta}_S$ is usually applied to boost the signal-to-noise ratio (SNR) in STEM imaging.

To confirm the necessity for a large STEM collection semi-angle $\boldsymbol{\beta}_S$ to eliminate bend contours, a range of values were explored. As shown in Figure 2a, when applying a small $\boldsymbol{\beta}_S$ of 0.3 mrad, similar to the TEM incidence semi-angle of 0.1 ~ 0.2 mrad for field-emission guns, bend contours emerged immediately in the STEM-BF image (indicated by solid red arrows). To put things in perspective, the 0.3 mrad $\boldsymbol{\beta}_S$ is drawn to the scale of the 6.2 mrad $\boldsymbol{\alpha}_S$ in the stationary STEM diffraction, illustrating that it collects only a very small fraction of the direct transmitted electron signal. Next, we increased $\boldsymbol{\beta}_S$ gradually (Figure 2b), and found that the bend contours in the STEM images effectively disappeared when $\boldsymbol{\beta}_S$ was increased to 3 mrad, about 15 times larger than the TEM incidence semi-angle $\boldsymbol{\alpha}_T$. This suggests that a reasonably large STEM collection angle is essential for suppressing bend contours in dislocation imaging.

(a) Sufficiently small STEM-BF collection angle β_S can recover bend contour

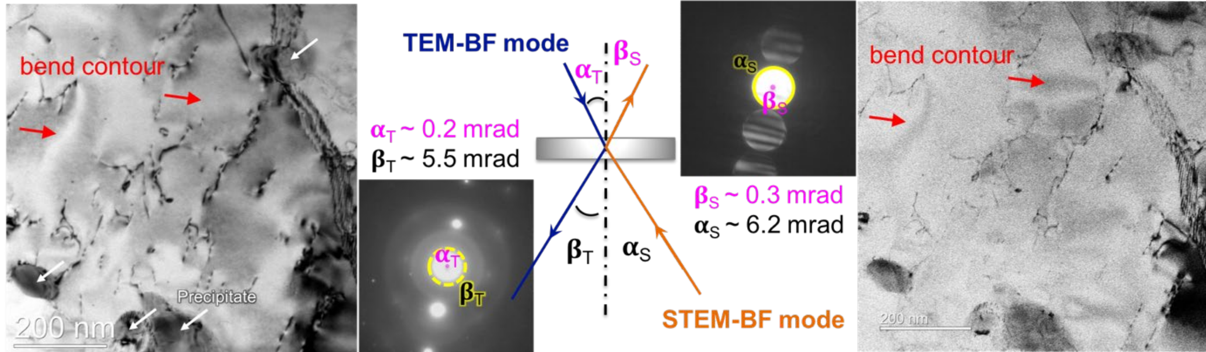

(b) Bend contour is suppressed when STEM β_S becomes comparable to α_S

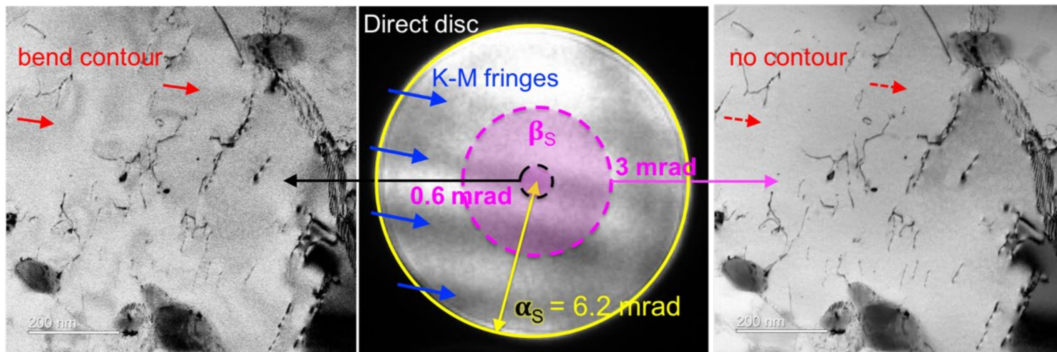

Figure 2. Schematic illustration of the influence of STEM bright field (BF) collection semi-angle $\boldsymbol{\beta}_S$ size on the presence of bend contours in dislocation imaging in STEM mode. (a) Ray diagram of CTEM and STEM BF images under strict reciprocity condition (i.e., $\boldsymbol{\alpha}_T \approx \boldsymbol{\beta}_S$ and $\boldsymbol{\beta}_T \approx \boldsymbol{\alpha}_S$). (b) A close-up of the parallel Kossel-Möllenstedt fringes (K-M fringes) in the direct disc (of a STEM stationary diffraction obtained away from dislocations) with the respect to two different $\boldsymbol{\beta}_S$ sizes, which are drawn to scale. Note that the CTEM-BF and STEM-BF images were recorded in a similar $\mathbf{g}_{011}$ systematic row diffraction condition for the HT-9 alloy.

The reason why $\boldsymbol{\beta}_S$ has such an effect on bend contours becomes obvious when considering its size with respect to the Kossel-Möllenstedt fringes (K-M fringes) in the direct STEM disc (Figure 2b). As we know, the parallel K-M fringes obtained under the systematic row diffraction condition in convergent-beam electron diffraction patterns reflect the rocking-curve intensity oscillation (as a function of TEM foil thickness) in reciprocal space, and are widely used for crystal thickness measurement [17]. When the STEM $\boldsymbol{\beta}_S$ is sufficiently small (e.g. smaller or comparable to the width of one K-M fringe), the corresponding local STEM image intensity (which is, in principle, integrated over the collection area with a radius of $\boldsymbol{\beta}_S$ in the direct disc) is subject to any variations in K-M fringe oscillation. For example, as shown in Figure 3a and 3b, an inspection of the K-M fringe patterns across a "bright-dark-bright" contour region found that although the overall number (nor width) of the K-M fringes does not change significantly across this local region, the position of the fringe pattern shifts with local foil tilt. Along with a small $\boldsymbol{\beta}_S$ here, this shift effectively reverses the intensity of the signals collected by the BF detector and leads to the presence of bend contours in STEM-BF images. In contrast, the same K-M fringe shift (or local foil bend) is invisible when $\boldsymbol{\beta}_S$ is increased to include multiple K–M fringes (Figure 2b, $\boldsymbol{\beta}_S$ = 3 mrad), for the oscillation between the dark fringes and the bright space in between is largely canceled out regardless of their positions. Thus, it results in a bend-contour-free dislocation image.

This leads to the following questions on the optimum STEM collection semi-angle β_S size and on if it compromises the dislocation contrast. While a lower limit of β_S size (~ 3 mrad) was discussed above to explain how DCI STEM evens out bend contours (K-M fringe oscillation) from the reciprocal space, in practice, we found a β_S comparable to the STEM convergence semi-angle α_S is optimum. In this way, the STEM BF detector collects the entire direct disc, offering uncompromised BF image SNR and more importantly preserving defect contrast in the simultaneous DF image (details will be discussed in Section 3.2 on the dependence of the camera length). And it is validated for a range of foil thickness from ~ 50 nm to ~ 250 nm, which is corresponding to ~ 1 to ~ 5 K–M fringes (typically one extinction distance per K-M fringe) for a ξ_{g011} of 42.2 nm at 200 kV for BCC Fe (details see Section 3.3). To address the second question, we looked into direct disc images obtained over dislocations lines and two examples are presented in Figure 3c. While Phillips et al. has provided computational validation of the $\boldsymbol{g} \cdot \boldsymbol{b}$ invisibility criteria in STEM mode [3], direct comparison between the weak K-M fringe (Figure 3b) and the strong Bragg lines (Figure 3c) shows that over dislocations the subsidiary maxima of the K-M fringes start to vanish and the intensity of the image is influenced only by the large excitation errors near the dislocation cores. For further quantitative discussion, structural models consisted of both bend contours and dislocations (with different $\boldsymbol{b}$ and $\boldsymbol{u}$) are necessary for image simulation, which is beyond the scope of this paper. We also noticed that the dislocation contrast in STEM imaging mode behaves very similar to that of under the CTEM mode, and the intensity of dislocations is optimum when the foil is tilted to approximately $1\mathbf{g}_{011}$ on Bragg (as adopted throughout this work).

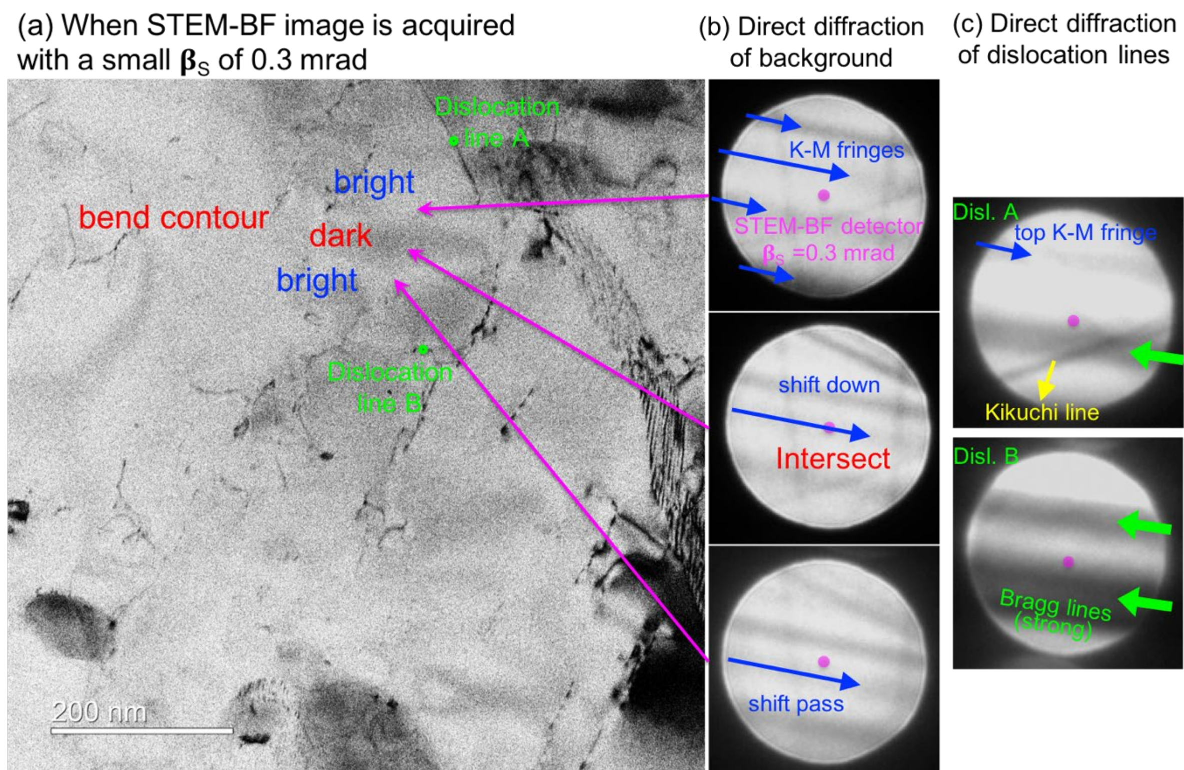

Figure 3. Inspection of the direct disc images in STEM stationary diffractions across regions presenting bend contours. (a) The STEM-BF image collected with a 0.3-mrad β_S in Figure 2b, and direct disc images when the STEM probe was on (b) the background with contours, and on (c) the dislocation line A and B (as marked in (a)). For the full diffractions patterns of (c) see Figure S2.

Other factors also play a role in eliminating bend contours in DCI STEM. As shown in the ray diagram in Figure 2a, although the size of the TEM collection angle $\boldsymbol{\beta}_T$ is several mrad, the TEM collection semi-angle $\boldsymbol{\alpha}_T$ remains small enough that it likely contains only one K-M fringe. This leads to a similar outcome to that of a small STEM collection $\boldsymbol{\beta}_S$ and the presence of bend contours. In contrast to STEM with a converged electron probe, the nature of parallel beam CTEM (i.e., small $\boldsymbol{\alpha}_T$) prevents it from accessing the rocking-curve oscillation in reciprocal space, meaning that one cannot eliminate bend contours easily in TEM mode. As discussed above that a STEM collection semi-angle $\boldsymbol{\beta}_S$ about an order larger than a typical TEM divergence semi-angle $\boldsymbol{\alpha}_T$ is necessary for suppressing bend contour, however, this does not mean the principle of reciprocity is broken. Instead, the "linear" nature of the reciprocity principle is unchanged, only that for STEM the angle of incidence is broadened opening up the possibility of mitigating the long range lattice bending. Thus, both reasonably large $\boldsymbol{\alpha}_S$ and $\boldsymbol{\beta}_S$ in a few mrad in STEM mode are necessary conditions for achieving bend-contour-free defect image.

3.2. Optimal STEM parameters for dislocation imaging

In this section, we examine the effects of different DCI STEM imaging parameters and sample conditions on dislocation images of a BCC ferritic alloy. The exact imaging parameters that work in one case might differ for other crystal systems; here, through systematic comparison, we aim at offering general guidelines.

Figure 4 presents the dislocation images of the same field of view obtained by CTEM and DCI STEM with different camera lengths. It is obvious that DCI STEM, in general, produces sharper and clearer images of the dislocation lines as well as the presence of precipitates and pseudo-grain boundaries. Among the DCI STEM attempts, we found a CL of 40 cm produced the best dislocation contrast in both STEM-BF and STEM-ADF images. Although the 120 cm STEM-BF image is almost as good as the 40 cm BF (with a slightly lower SNR), the dislocation contrast is faded in the simultaneous ADF image because the resulting small ADF inner collection angle includes a strong contribution from the direct disc, subsequently smearing the signals from the diffraction discs. On the other hand, the smaller 12 cm CL leads to the similar issue of mixing the directly transmitted signal with the diffracted signals in BF imaging. In this case, since Bragg lines in diffraction discs $\pm\mathbf{g}$ exhibit a reversed intensity of the lines in the direct disc (Figure S2) the integrated image intensity (over both diffracted and direct disc) over dislocations is reduced, leading to fading dislocation contrast in the BF image. Meanwhile, the corresponding high ADF collection semi-angle excludes the strong low-order diffraction discs and gives ambiguous dislocation contrast. A CL of 80 cm was also tested (Figure S3). Although it better satisfies the criterion for BF collection (< 6.2 mrad of the $\boldsymbol{\alpha}_S$), the ADF image includes the 1$\mathbf{g}$ disc and a part of the 2$\mathbf{g}$ diffraction disc, producing a more diffuse dislocation contrast than that collected using CL = 40 cm (including diffraction discs up to 3$\mathbf{g}$). This also shows that an outer BF collection semi-angle slightly larger than the direct disc does not cause notable changes in the dislocation contrast, because the strong direct transmitted signal remains the dominant contribution to the STEM image contrast. Nevertheless, if we are only concerned about STEM-BF dislocation images as typically used in CTEM, the choice of CL is less restrictive (e.g., from 12 cm to 120 cm in this case) as long as it provides a reasonably large $\boldsymbol{\beta}_S$ to suppress bend contours.

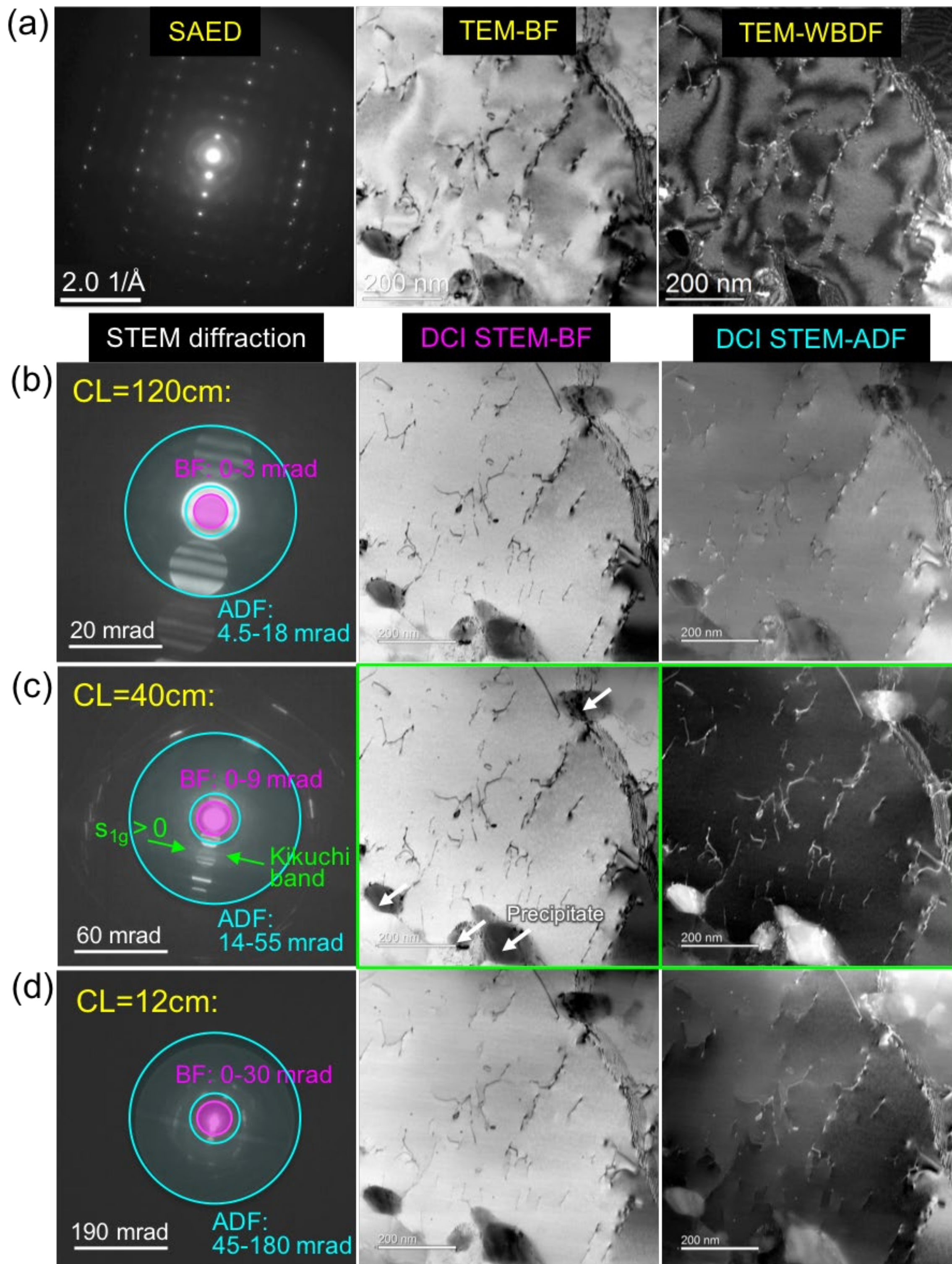

Figure 4. Dependence on the camera length (collection range) of DCI STEM dislocation imaging. The diffraction, BF and DF images in (a) the CTEM imaging mode, and in the DCI STEM mode with camera lengths of (b) 120 cm, (c) 40 cm, and (d) 12 cm of the same field of view under the a similar $\mathbf{g}_{011}$ systematic row diffraction condition. $\boldsymbol{\alpha}_S$ was kept at 6.2 mrad. The corresponding BF and ADF detector collection ranges are illustrated to scale in the STEM diffractions. Green frames outline the preferred STEM setting.

Next, we tested the effects of different STEM convergence semi-angles ($\boldsymbol{\alpha}_S$). As mentioned in Section 2.2, the size of $\boldsymbol{\alpha}_S$ should not exceed the first-order diffraction size to avoid STEM

disc overlap based on STEM image contrast theory [18]. However, this might not seem very obvious from the CTEM point of view. Here, we confirmed this criterion by performing direct comparison over the same field of view with a series of $\boldsymbol{\alpha}_S$ semi-angle sizes of 6.2, 13.1, and 27.5 mrad, and the results are presented in Figure 5. For a fair comparison, the camera length was kept the same (40 cm). For the 6.2-mrad $\boldsymbol{\alpha}_S$ with non-overlapping STEM diffraction discs, the corresponding DCI STEM-BF and -ADF pairs suppress the intensive bend contours present in the CTEM counterpart, providing a much sharper picture of line dislocations and of a nearby low angle grain boundary. As $\boldsymbol{\alpha}_S$ increases (Figure 5c and 5d), the $\mathbf{g}_{011}$ diffraction discs start overlapping. This leads to the contrast of some dislocation lines fading away in the STEM-BF images. Moreover, the STEM-ADF images show obvious degradation with increasing $\boldsymbol{\alpha}_S$. Even though the 13.1-mrad ADF is free from the strong signals from the direct disc, extra intensities arise from the overlapping diffraction discs and in other parts of reciprocal space that also fall onto the ADF detector. These contributions from the overlap and non-diffraction disc smear the dislocation contrast in ADF images. Thus, the question becomes, is large-$\boldsymbol{\alpha}_S$ DCI STEM-BF imaging desirable? After careful inspection of the dislocations in the three BF images, we found that the intensity of some dislocation lines (in broken blue circles) was reduced significantly as $\boldsymbol{\alpha}_S$ was increased to 27.5 mrad. Considering that the depth of field is inversely dependent on $\boldsymbol{\alpha}_S$ [19], a large $\boldsymbol{\alpha}_S$ leads to a short depth of field that causes defocus at the outer edges of the image (Figure S4). Thus, the optimal STEM convergence semi-angle not only precludes diffraction disc overlap, but it also offers a larger depth of field that produces a more uniformly focused image.

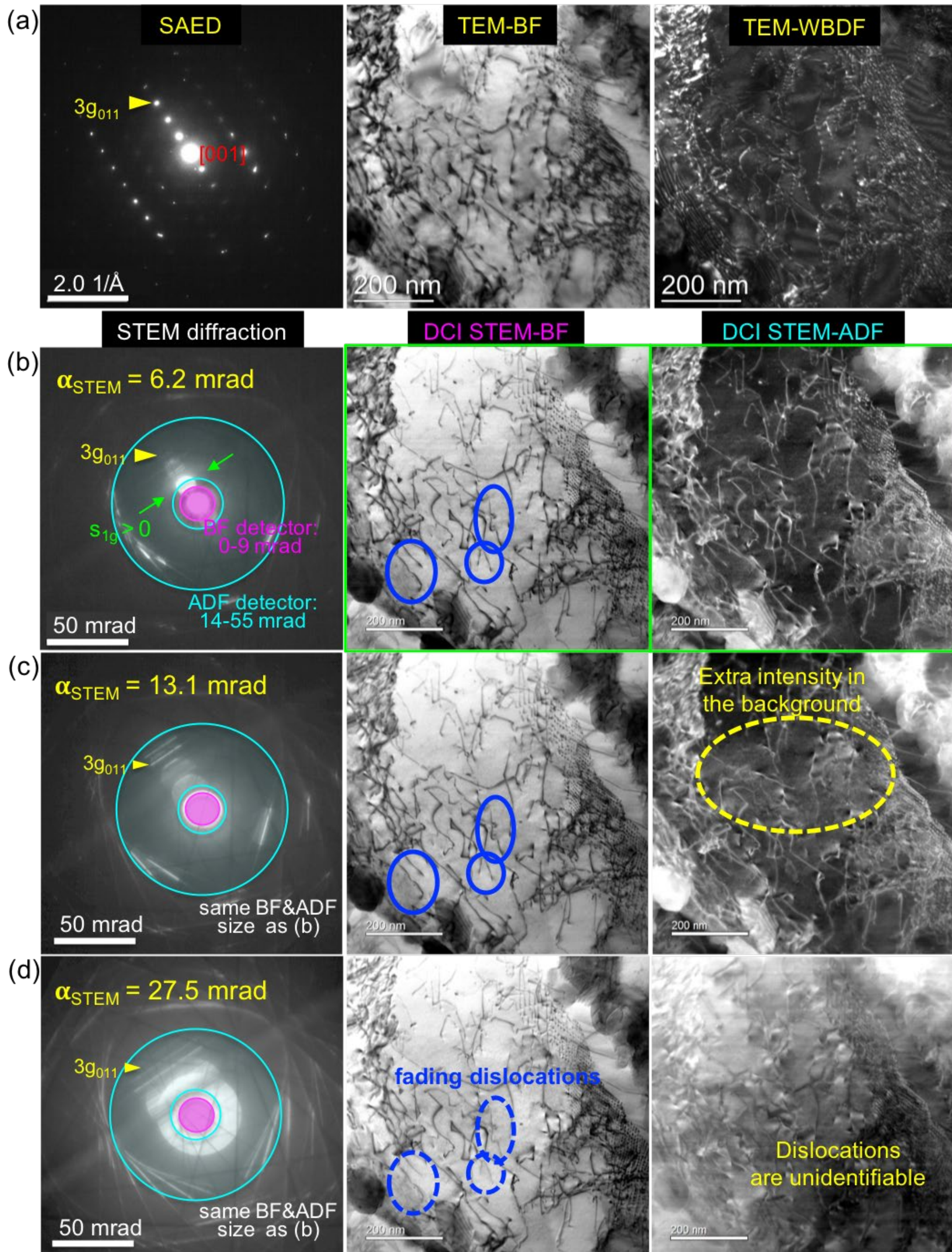

Figure 5. Dependence on the convergence angle of DCI STEM dislocation imaging. The diffraction, BF and DF images in (a) the CTEM imaging mode, and in the DCI STEM mode with a probe semi-angle of (b) $\boldsymbol{\alpha}_S$ = 6.2 mrad, (c) $\boldsymbol{\alpha}_S$ = 13.1 mrad, and (d) $\boldsymbol{\alpha}_S$ = 27.5 mrad of the same field of view under a similar $\mathbf{g}_{011}$ systematic row diffraction condition. Green frames outline the preferred STEM settings.

To find out whether the quality of DCI STEM images could be further optimized, we tested different sizes and positions of the objective aperture, as well as shifting the diffracted beam to the STEM-BF detector (similar to the WBDF CTEM). Figure 6 shows the comparison among CTEM, "standard" DCI STEM, and the effects of detector and objective aperture. Again, compared to the matching CTEM images, both STEM-BF and -ADF in Figure 6b yield a sharper contrast for the dislocations, the nearby grain boundaries, and the precipitates. In Figure 6c, the $1\mathbf{g}_{011}$ STEM diffraction disc was shifted to the center of the STEM-BF detector using the projector lens to mimic the beam tilt operation in the WBDF mode. The resulting STEM-BF image does not provide the equivalent contrast to the WBDF CTEM. Instead, it presents an ADF characteristic since the BF detector is collecting the $1\mathbf{g}$ diffraction signals. The corresponding ADF image, similar to the ADF images in Figures 4b and 5d, shows reduced dislocation contrast due to the interaction between the strong transmitted beam and the diffraction discs on the ADF detector. Neither case suggests optimization.

On the other hand, the use of the objective aperture in STEM-ADF imaging further improved the dislocation contrast. A previous study has shown that the position of the objective aperture could affect the contrast of STEM images of stacking faults [12]. Here we tested different aperture sizes and positions of objective apertures, concluding that the best contrast for dislocations was achieved for the insertion of a 15.6 mrad aperture (~2.5 times $\boldsymbol{\alpha}_S$) on the $3\mathbf{g}_{011}$ diffraction disc (Figure 6d). In this case, the objective aperture selectively includes only the first three $\mathbf{g}_{011}$ reflections from the BCC crystal. This yielded perhaps the best dislocation contrast, with sharp contrast and no bend contours, thickness fringes, or other competing contrast mechanisms. However, the neighboring grains oriented differently from the central grain are not visible, implying the choice and positioning of the objective aperture did not capture any diffraction spots from those features. To gain a quantitative insight into the effects of the size and position of the objective aperture on dislocation imaging, we calculated the image contrast and SNR of a few dislocation lines. One representative result is presented in Figure 7. As shown in Figure 7e, the intensity line profiles of a chosen dislocation line (marked in Figure 7a) after normalized to the initial background intensity, show that the "standard" DCI STEM-BF image (no aperture, in magenta) provides the highest dislocation contrast (i.e. the net peak height). We then define the SNR as this contrast divided by the standard deviation of the background intensity (Figure S5), such that the higher the SNR the better the imaging ability to observe the defect feature [7]. And the results (as marked in Figure 7a-7c) show that the 15.6-mrad aperture positioned over $3\mathbf{g}_{011}$ offers the highest SNR. For the abnormal contrast observed in Figure 7c and Figure 6d when the 5.5-mrad aperture selects only the $3\mathbf{g}_{011}$ disc, it can be probably relieved by tilting the TEM foil to $\mathbf{s}_{3\mathbf{g}} = 0$ [3]. Other dislocation lines (with a different $\boldsymbol{b}$ and $\boldsymbol{u}$), though present different values of contrast and SNR, they share a similar trend as the one in Figure 7. In sum, if dislocations are the sole interest of a study, the application of a 15.6 mrad objective aperture over the $3\mathbf{g}_{011}$ boosts the SNR of the resulting dislocation image; whereas, if it is desired to include these other microstructural features such as precipitates and defects in neighboring grains, then the "standard" DCI STEM images (Figure 6b and 7a), i.e., no objective apertures used, provides a more complete picture of the microstructural features.

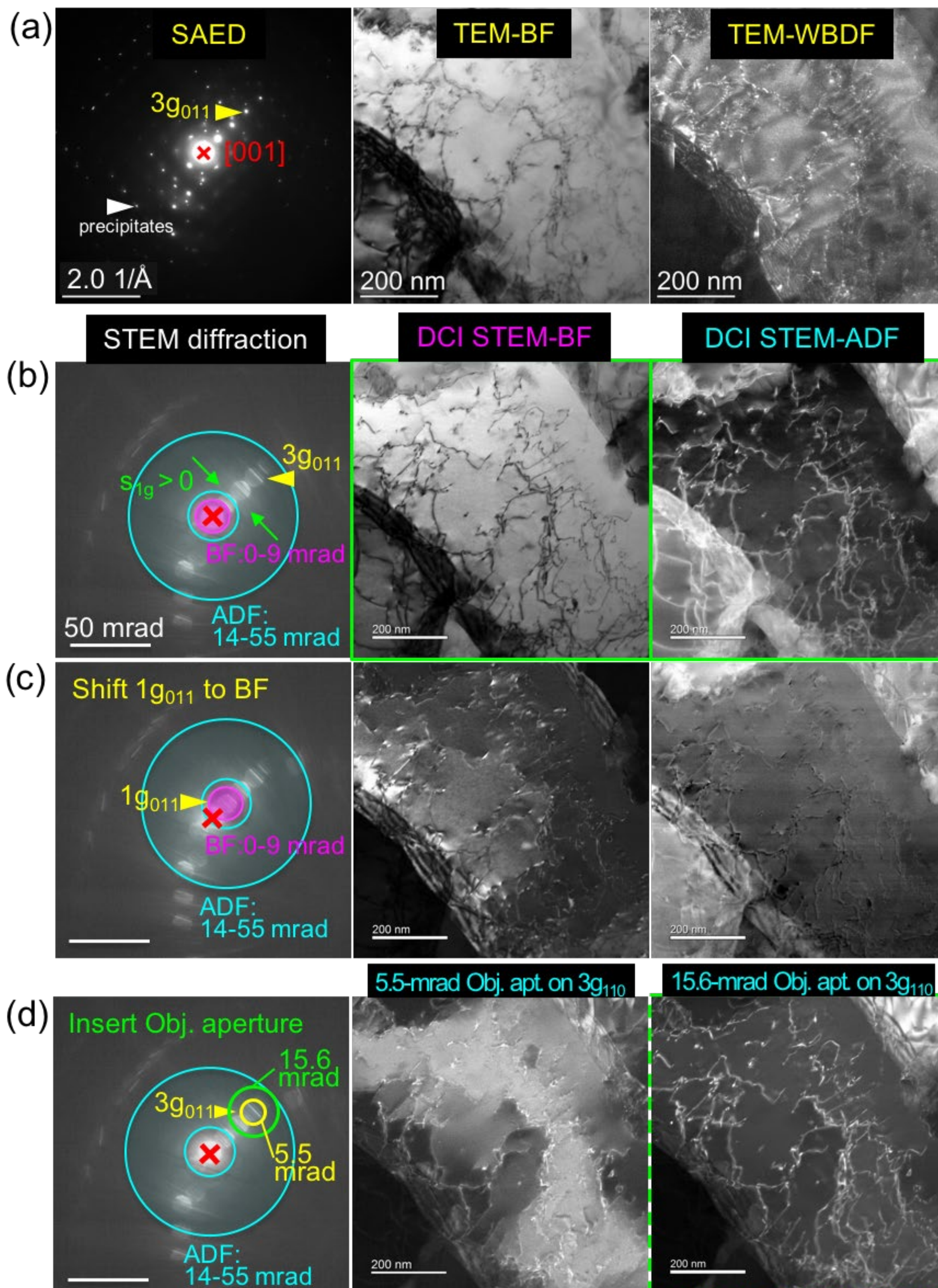

Figure 6. Dependence on STEM detector and objective aperture of DCI STEM dislocation imaging. The diffraction, BF and DF images in (a) the CTEM imaging mode, (b) the "standard" DCI STEM mode (same as Figure 1), and in (c) the DCI STEM with $1\mathbf{g}_{011}$ shifted to BF, and (d) DCI STEM-ADF with objective apertures over $3\mathbf{g}_{011}$. All STEM images were obtained using $\boldsymbol{\alpha}_S$ = 6.2 mrad, CL = 40 cm as optimized above. Green frames outline the preferred STEM settings.

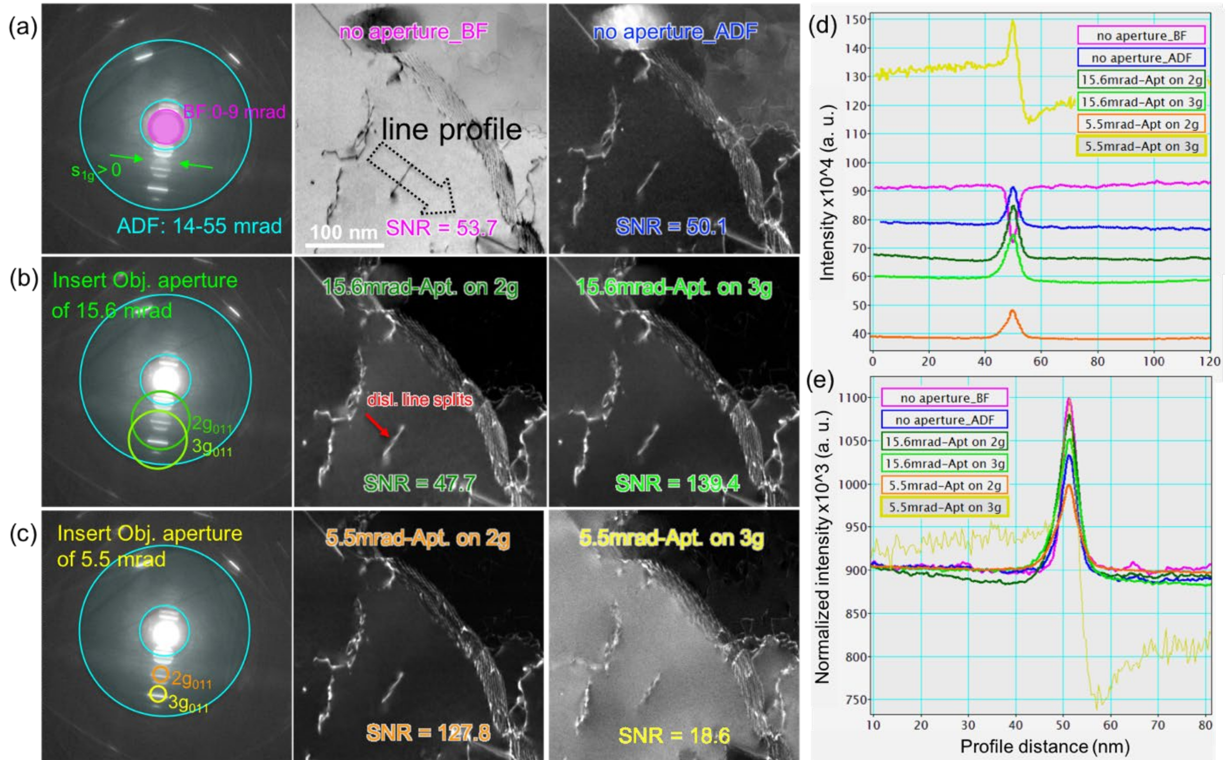

Figure 7. Quantitative comparison of image intensity and signal-to-noise radio (SNR) of a dislocation line under the condition of (a) the “standard” DCI STEM mode (no aperture), (b) the 15.6-mrad and (c) the 5.5-mrad objective aperture over the center of the $2\mathbf{g}_{011}$ and $3\mathbf{g}_{011}$ diffraction disc, respectively. (d) Raw intensity line profiles across the chosen dislocation line (marked by a dashed arrow in the BF image in (a)) under different imaging conditions. (e) Intensity line profiles in (d) normalized to the initial background intensity. All STEM images were obtained using $\boldsymbol{\alpha}_S = 6.2$ mrad, CL = 40 cm, and under the same systematic row diffraction of approximately $\mathbf{s}_{1\mathbf{g}} = 0$. For calculations of SNR see Figure S5.

3.3. Effects of sample orientation and thickness on STEM dislocation imaging

Using the optimized DCI STEM settings, we first examined the effect of different sample orientations on the DCI STEM dislocation imaging contrast. Figure 8 presents the DCI STEM images obtained under the standard $\mathbf{g}_{011}$ systematic row condition with foil tilted approximately $\mathbf{s}_{1\mathbf{g}} = 0$ [3], a modified systematic row condition using $\mathbf{g}_{002}$, and the on-zone condition of $\mathbf{z}$ = [001] over a field of view containing a mixture of microstructural features. The first-row images stand out for the more uniform background intensity as well as the refined contrast of the dislocation lines. Under this diffraction condition, the distributions of all defects including dislocations, precipitates, and the pseudo-grain boundaries in this region are well resolved and easily identifiable. The different diffraction contrast presented in the two condition images can be understood by comparing the extinction distance ξ_g for the two systematic row diffraction vectors $\mathbf{g}_{011}$ and $\mathbf{g}_{002}$. Based on the definition of extinction distance ξ_g, the value of ξ_g varies for different $\mathbf{g}$ (and thus the Bragg angles) [20]. For example, in the case of BCC Fe, the ξ_g is about 42.2 nm for $\mathbf{g}_{011}$, while it is 60.8 nm for $\mathbf{g}_{002}$ at 200 kV. Since the diffraction contrast details are usually enhanced by reducing the value of ξ_g [8], the smaller ξ_g for $\mathbf{g}_{011}$ is more advantageous than the $\mathbf{g}_{002}$ for diffraction imaging. Moreover, although zone axis DCI STEM images have shown reasonable contrast for resolving stacking faults and dislocations in regions

free of other defects [3, 8], the on-zone image in Figure 8c shows diffuse dislocation contrast, and the particles are not as easily distinguishable in this field of view. Thus, while on-zone DCI STEM imaging could be beneficial for simple crystals, in materials with a high density of extended microstructural defects, the systematic row diffraction condition may yield a clearer picture by removing some of the extended defects through the $\boldsymbol{g} \bullet \boldsymbol{b}$ invisibility criteria.

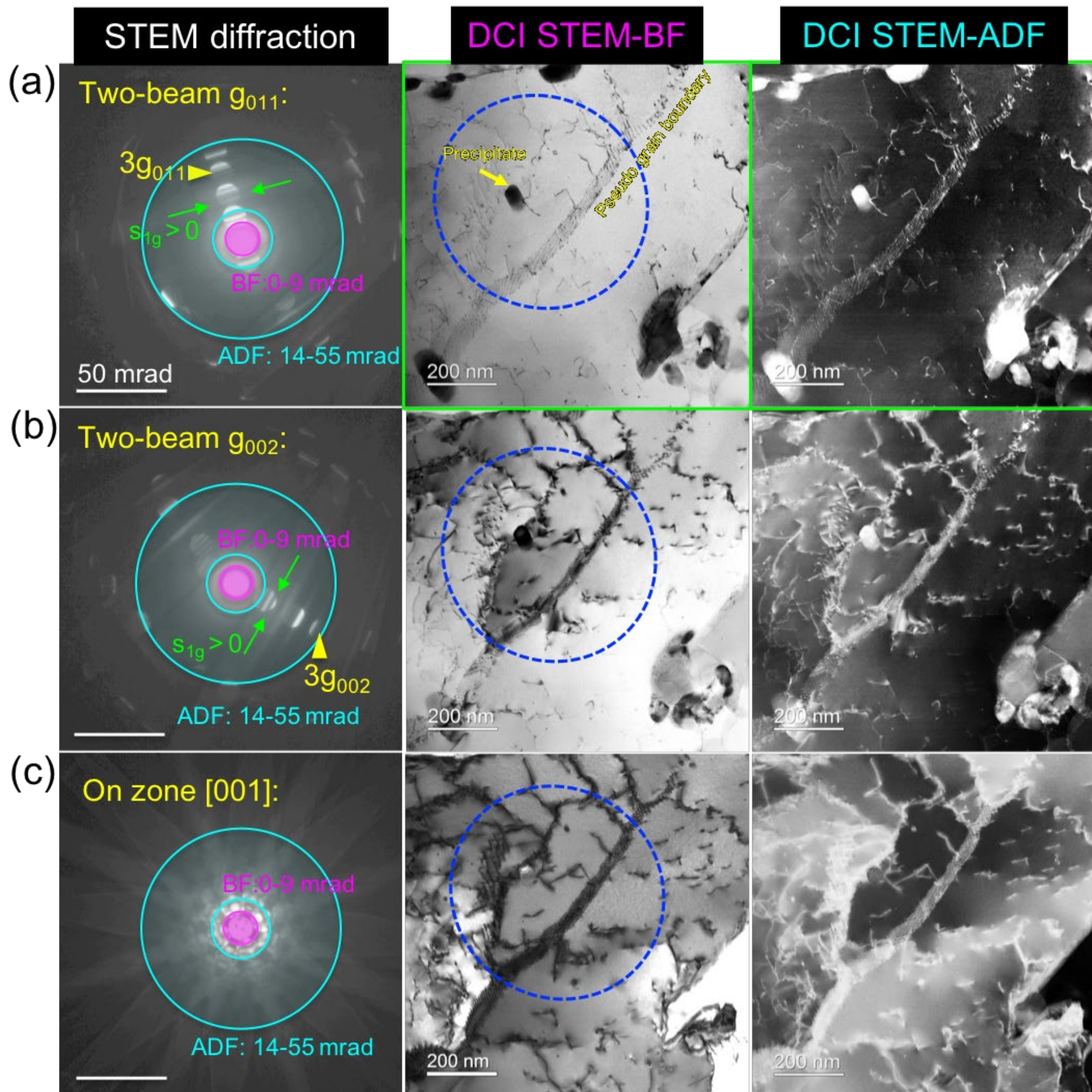

Figure 8. Dependence on sample orientation of DCI STEM dislocation imaging. The STEM diffraction, BF, and ADF images of (a) the standard $\mathbf{g}_{011}$ systematic row condition, (b) a modified $\mathbf{g}_{002}$ systematic row condition, and (c) on the zone axis of [001]. For corresponding CTEM images, see Figure S6. All STEM images were obtained using $\boldsymbol{\alpha}_S$ = 6.2 mrad, CL = 40 cm as optimized above without objective aperture. Green frames outline the preferred STEM settings for the BCC ferritic alloy studied here.

CTEM and optimized DCI STEM dislocation images as a function of TEM foil thickness are presented in Figure 9. As indicated by the red arrows, the bend contours blurring the dislocation contrast are largely alleviated even for the thin region of 55 nm. While a local

contour still presents at the top left of the DCI STEM-BF image (pointed by a horizontal solid arrow) likely due to local foil tilt, the visibility of the dislocation lines is improved compare to that of in the CTEM and the middle region is free of contours. This demonstrates the effectiveness of the optimized DCI STEM for thin foils with few K-M fringes. For the thick region (~240 nm) that has a higher apparent dislocation density, the DCI STEM images also offer well-resolved dislocations and precipitates with sharp contrast, particularly for the bent region near the bottom. A previous study suggested that the converged electron probe in STEM mode provides a cone in reciprocal space with an opening angle of 2α_S [21]. This cone defines a range of Ewald spheres that can accommodate displaced reciprocal lattice points due to bending, e.g., near the core of a dislocation. This observation confirms that the advantages of DCI STEM imaging are preserved for thick samples, as reported by Phillips et al. [12].

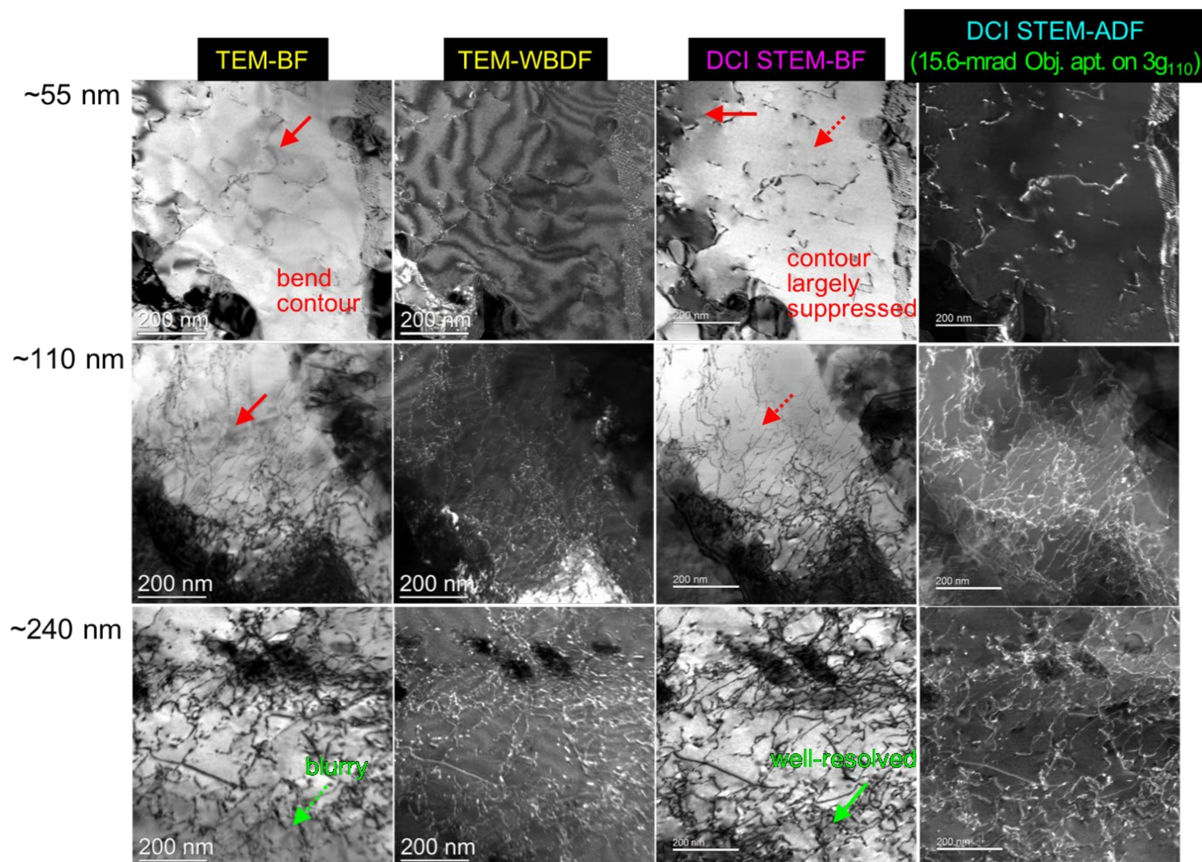

Figure 9. Dependence on sample thickness of DCI STEM dislocation imaging. CTEM and DCI STEM images of 55 nm, 110 nm, and 240 nm thick sample regions. As optimized above, all STEM images were obtained using α_S = 6.2 mrad, CL = 40 cm, with the 15.6 mrad objective aperture over 3$\mathbf{g}_{011}$ for ADF imaging. For corresponding electron diffractions, see Figure S7. The TEM foil thickness was measured by STEM-EELS spectrum imaging, and the marked thickness values are averaged over the field of view.

3.4. Comprehensive STEM-based characterization for alloy study

As the DCI STEM imaging technique has been established and optimized above, now it is beneficial to take advantage of the associated analytical techniques that can be performed in tandem with DCI-STEM imaging to provide a comprehensive microstructural and chemical characterization. An example workflow is schematically illustrated in Figure 10. Considering

that foil thickness is important for an accurate estimation of dislocation density, and that the excitation volume for STEM-EDS analysis depends on foil thickness [11], STEM-EELS zero-loss spectroscopy is the first step to provide the TEM foil thickness distribution [14]. Next, DCI STEM dislocation imaging is conducted in selected regions with suitable foil thickness. Over the same sample region, STEM-EDS is then performed to provide complementary chemical information in the area of interest. Overlaying the EDS elemental maps on the dislocation images, important questions such as the interplay between dislocations and a certain type of precipitates, or a relationship between potential chemical segregations and (pseudo-) grain boundaries can be explored. Also, this streamlined characterization would facilitate comparison among alloys in different conditions.

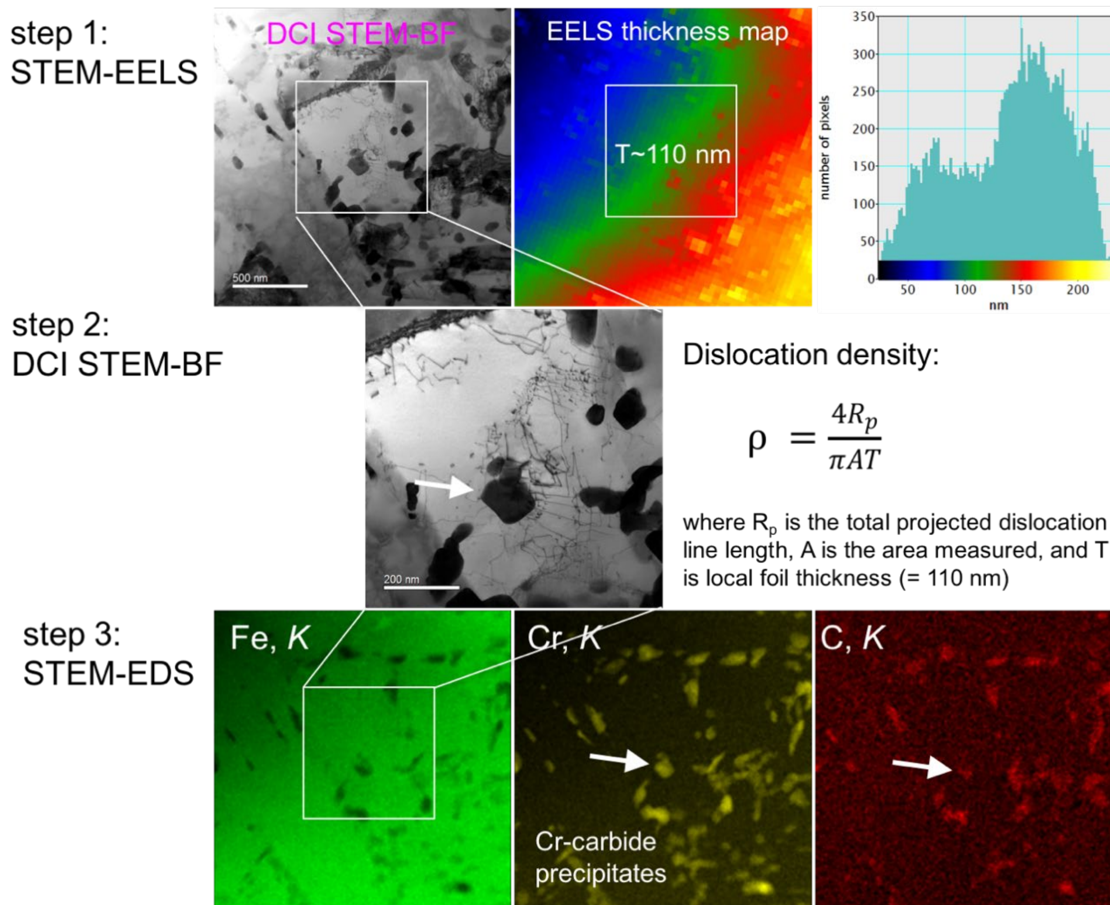

Figure 10. The workflow of a comprehensive defect characterization in STEM mode.

4. Conclusion

In this work, we investigated why DCI STEM suppresses bend contours and auxiliary contrast and leads to a better dislocation imaging. Based on the findings, we explored how to set up and optimize DCI STEM parameters for a given crystalline specimen. The image formation process in the STEM mode suggests that both the STEM convergence and collection semi-angles, α_S and β_S, respectively, need to be reasonably large (around a few mrad) to alleviate the bend contours that often dominate in the background contrast of CTEM dislocation images. Unlike the parallel electron beam in CTEM, the converged STEM electron probe opens up a cone in reciprocal space that accesses the rocking-curve oscillation; then a

sufficiently large **β**s (~ **α**s) behaves like a "mask" averaging out this oscillation, leading to a uniform background when imaging dislocations. It is particularly powerful in resolving complex microstructures containing a high density of dislocations, grain boundaries, and precipitates.

Using a BCC ferritic alloy specimen, optimized DCI STEM image conditions were identified that appear to work well for complicated microstructures with dense defects. This includes a convergence semi-angle that yields a converged probe that prevents STEM disc overlap, a camera length that offers a BF collection semi-angle similar to the radius of the direct transmitted disc, and an ADF inner/outer angle that excludes the direct disc while including diffraction discs up to 3**g**. And finally, the orientation of the specimen is preferably in a systematic row condition using a 1**g** vector with a small extinction distance and the TEM foil tilted to a small positive excitation error. An objective aperture centered around a high-order 3**g** diffraction disc can further refine the contrast for the dislocations satisfying the Bragg condition. Relatively thick foils do not significantly degrade the DCI STEM image quality, an inherent advantage over CTEM images, which are usually limited to < 200 nm of foil thickness for any appreciable dislocation density (~ 10^{15} per m^2). Thus, the improvement in dislocation imaging coupled with the ability to simultaneously capture chemical information in STEM mode allows a faster, more thorough comprehensive characterization of crystallographic defects and chemical information in a single imaging mode.

Acknowledgments

This research is supported by the U.S. Department of Energy Office of Nuclear Energy's Nuclear Energy Enabling Technologies program project CFA 16-10570 at Pacific Northwest National Laboratory and by the Office of Fusion Energy Sciences under contract DE-AC05-76RL01830. Colin Ophus' work at the Molecular Foundry was supported by the Office of Basic Energy Sciences, of the U.S. DOE under Contract No. DE-AC02-05CH11231. The authors thank Dr. Larry Thomas and Dr. Libor Kovarik for fruitful and insightful discussions on diffraction contrast. We also thank Michael Mills for his thought-provoking presentations and discussions of the DCI STEM technique. A portion of the research was performed using the Environmental Molecular Sciences Laboratory (EMSL), a national scientific user facility sponsored by the Department of Energy's Office of Biological and Environmental Research and located at Pacific Northwest National Laboratory.

References

[1] P.B. Hirsch, R.W. Horne, M.J. Whelan, Direct observations of the arrangement and motion of dislocations in aluminum, Philosophical Magazine, 1 (1956) 677-&.
[2] W. Bollmann, Interference effects in the electron microscopy of thin crystal foils, Physical Review, 103 (1956) 1588-1589.
[3] P.J. Phillips, M.C. Brandes, M.J. Mills, M. De Graef, Diffraction contrast STEM of dislocations: Imaging and Simulations, Ultramicroscopy, 111 (2011) 1483-1487.
[4] K. Yoshida, M. Shimodaira, T. Toyama, Y. Shimizu, K. Inoue, T. Yoshiie, K.J. Milan, R. Gerard, Y. Nagai, Weak-beam Scanning Transmission Electron Microscopy for quantitative dislocation density measurement in steels, Microscopy, 66 (2017) 120-130.
[5] Y. Zhu, C. Song, A.M. Minor, H. Wang, Cs-Corrected Scanning Transmission Electron Microscopy investigation of dislocation core configurations at a SrTiO3/MgO heterogeneous interface, Microsc. Microanal., 19 (2013) 706-715.

[6] Y. Zhu, C. Ophus, J. Ciston, H. Wang, Interface lattice displacement measurement to 1 pm by geometric phase analysis on aberration-corrected HAADF STEM images, Acta Mater., 61 (2013) 5646-5663.
[7] Y. Zhu, N.D. Browning, The role of gas in determining image quality and resolution during in situ Scanning Transmission Electron Microscopy experiments, ChemCatChem, DOI: 10.1002/cctc.201700474 (2017) 1.
[8] D.M. Maher, D.C. Joy, Formation and interpretation of defect images from crystalline materials in a scanning-transmission electron-microscope, Ultramicroscopy, 1 (1976) 239-253.
[9] K.E. Easterling, Metallurgical applications of scanning-transmission electron-microscopy, Journal of Materials Science, 12 (1977) 857-868.
[10] C.J. Humphreys, Fundamental-concepts of stem imaging, Ultramicroscopy, 7 (1981) 7-12.
[11] C.M. Parish, K.G. Field, A.G. Certain, J.P. Wharry, Application of STEM characterization for investigating radiation effects in BCC Fe-based alloys, J. Mater. Res., 30 (2015) 1275-1289.
[12] P.J. Phillips, M.J. Mills, M. De Graef, Systematic row and zone axis STEM defect image simulations, Philosophical Magazine, 91 (2011) 2081-2101.
[13] E.J. Kirkland, The Transmission Electron Microscope, in: Advanced Computing in Electron Microscopy, Springer, 2010, pp. 18.
[14] T. Malis, S.C. Cheng, R.F. Egerton, EELS log-ratio technique for specimen-thickness measurement in the TEM, J Electron Microsc Tech, 8 (1988) 193-200.
[15] J.M. Cowley, Image contrast in a transmission scanning electron microscope, Appl. Phys. Lett., 15 (1969) 58-&.
[16] A.P. Pogany, P.S. Turner, Reciprocity in electron diffraction and microscopy, Acta Crystallographica Section a-Crystal Physics Diffraction Theoretical and General Crystallography, A 24 (1968) 103-&.
[17] D. Delille, R. Pantel, E. Van Cappellen, Crystal thickness and extinction distance determination using energy filtered CBED pattern intensity measurement and dynamical diffraction theory fitting, Ultramicroscopy, 87 (2001) 5-18.
[18] P.D. Nellist, S.J. Pennycook, The principles and interpretation of annular dark-field Z-contrast imaging, in: P.W. Hawkes (Ed.) Advances in Imaging and Electron Physics, Elsevier, 2000, pp. 147-203.
[19] A.Y. Borisevich, A.R. Lupini, S. Travaglini, S.J. Pennycook, Depth sectioning of aligned crystals with the aberration-corrected Scanning Transmission Electron Microscope, J. Electron Microsc., 55 (2006) 7-12.
[20] David B. Williams, C.B. Carter, Diffracted Beams, in: Transmission Electron Microscopy: A Textbook for Materials Science, Springer US, 2009, pp. 223-224.
[21] L.A. Jacome, G. Eggeler, A. Dlouhy, Advanced scanning transmission stereo electron microscopy of structural and functional engineering materials, Ultramicroscopy, 122 (2012) 48-59.